Available online at www.sciencedirect.com
SCIENCE DIRECT®
Sensors and Actuators A 119 (2005) 476–488
SENSORS AND ACTUATORS A PHYSICAL
www.elsevier.com/locate/sna

Optimal energy density piezoelectric bending actuators

R.J. Wood*, E. Steltz, R.S. Fearing

Department of EECS, University of California at Berkeley, 211 Cory Hall 1772, Berkeley, CA 94720, USA

Received 14 June 2004; received in revised form 6 October 2004; accepted 17 October 2004
Available online 8 December 2004

Abstract

The design and analysis of piezoelectric actuators is rarely optimized for low mass applications. However, emerging technologies such as micro air vehicles, and microrobotics in general, demand high force, high displacement, low mass actuators. Utilization of generic piezoceramics and high performance composite materials coupled with intelligent use of geometry and novel driving techniques yields low cost, rapidly prototyped, ultra-high energy density bending actuators for use in such applications. The design is based upon a laminate plate theory model for a stacked multimorph cantilever actuator, encompassing all possible layups, layer anisotropies, internal and external excitations, and intrinsic and extrinsic geometries. Using these principles, we have fabricated 12 mg PZT bimorph actuators with greater than $2\,J\,kg^{-1}$ energy density. This gives a performance increase of an order of magnitude or greater compared to existing commercially available piezoelectric bending actuators.

Keywords: Piezoelectric actuators; Microactuators; Bimorph; Composites

1. Introduction

This work addresses a number of key points in actuator design, specifically for high energy density applications, which are unique among the design of transducers. The overall goal of this paper is to describe methods for creating bending actuators which result in each infinitesimal electro-active element having a strain close to its ultimate strain for a given set of known internal and external excitations. In total, three coupled techniques are described here for increasing the energy density of clamped-free piezoelectric bending actuators: geometry, smart material choices, and optimal high field driving techniques. Each individually gives an improvement over existing competitors, however when coupled together the result is a factor of 10 or greater energy density improvement. As a verification of the model and fabrication process, this work develops and tests a millimeter-scale bimorph actuator and compares the results to existing bending actuators.

One novelty of the approaches presented here is the modeling of the actuator performance, both of the actuator output and of the interactions between internal and external excitations. There have been numerous models presented for the mechanics of rectangular piezoelectric transducers. DeVoe and Pisano [4] presented a model for MEMs cantilever actuators considering multiple passive layers. Smits and Ballato [13], Smits and Choi [14] and Weinberg [18] described in detail a one-dimensional analysis of piezoelectric bending actuator performance using energy methods. More specific to this work, Wang and Cross [16] modeled a bimorph with a central passive layer and the effects thereof. For microrobotics applications, Sitti et al. [12] described the design of millimeter scale bending actuators. For greater generality, laminate plate theory is used in this work to describe the interaction between the external and internal forces and moments with the layer stresses and strains. This not only predicts the displacement and blocked force of the actuator, but additionally the strains in each layer for failure analysis as well. Although the discussion in this paper is

* Corresponding author. Tel.: +1 510 6435796; fax: +1 510 6427644.
E-mail addresses: rjwood@eecs.berkeley.edu (R.J. Wood); ees132@eecs.berkeley.edu (E. Steltz); ronf@eecs.berkeley.edu (R.S. Fearing)

0924-4247/$ – see front matter © 2004 Elsevier B.V. All rights reserved.
doi:10.1016/j.sna.2004.10.024

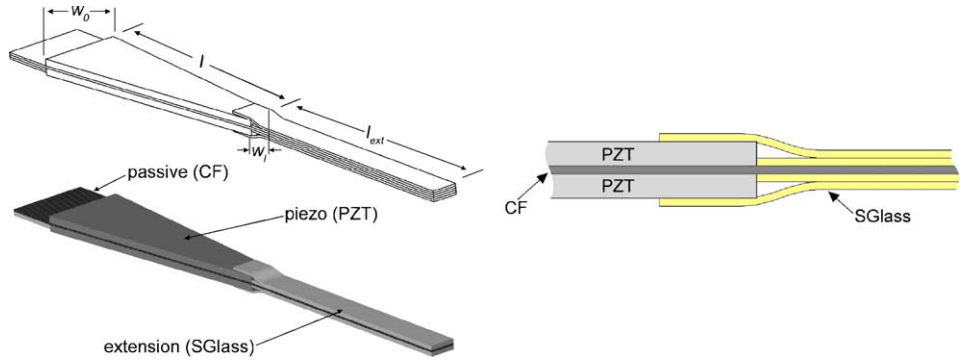

Fig. 1. Bimorph drawing with pertinent dimension descriptions.

concentrated on piezoelectric actuation, this model is easily adapted to thermally excited and other electro-active actuators as well. The use of actively or passively (elastically) anisotropic constituent layers can also yield interesting tailored kinematics (bending-twisting and extension-twisting coupling for example) and is also encompassed within this model.

There are a number of existing and conceptual applications for such a technology, for example as the flight muscles for a flapping wing micro air vehicle [21], control surface actuators for indoor slow fliers [6,9], motors for micro legged robots [5], drivers for haptic display devices [11], etc.

1.1. Design preliminaries

Fig. 1 shows a drawing of the proposed bimorph actuator for design purposes. Note that the width is tapered along the length; the actuator geometry will be discussed in Section 2.1. Also, the elastic (passive) material is drawn as one layer. In reality, however, it could be composed of a number of layers in arbitrary orientations as will be discussed in Section 2. The effects of an extension will be described in Section 2.2. For performance comparisons, the mechanical energy is defined as the area under the force–displacement curve:

$$U_m = \tfrac{1}{2} F_\mathrm{b} \delta_\mathrm{max} \tag{1}$$

where F_b and δ_max are the peak-to-peak blocked force and unloaded maximum tip displacement respectively for a given field. This paper assumes that the actuators are driven quasi-static ($f \ll f_0$), thus the power is a linear function of the drive frequency. However for such actuators driving resonant systems ([2,20,21]) the power able to be delivered to a given load is a function of internal dissipations. The dissipation effects on the power delivery capabilities for resonant systems are quantified in Eq. (2).

$$P = \begin{cases} \frac{1}{8} 2\pi f_0 F_\mathrm{b} \delta Q_\mathrm{l} & \text{for } Q_\mathrm{a} \gg Q_\mathrm{l} \\ \frac{1}{16} 2\pi f_0 F_\mathrm{b} \delta Q & \text{for } Q_\mathrm{a} \approx Q_\mathrm{l} \end{cases} \tag{2}$$

In Eq. (2) f_0 is the total system resonant frequency and the mechanical Q is a function of the lumped system stiffness, mass, and loss: $Q = \sqrt{km}/b$. This paper does not address actuator and load dynamics and losses and thus the energy density will be the performance merit for the remainder of this discussion.

Table 1 lists the specifications of current commercially available actuators. Note that the magnitudes of the applied fields in Table 1 for the first two actuators are small compared

Table 1
Commercially available clamped-free cantilever piezoelectric bending actuator specifications

Actuator	δ_max[a] (μm)	F_b[a] (mN)	m (mg)	D_U (J kg^{-1})	Field[b] (V μm^{-1})	Piezo material[c]
T219-H4CL-103X[d]	610	160	320	0.153	0.25	5H
QP21B[e]	790	460	2800	0.065	0.50	5A
TH-8R[f]	1900	111	1780	0.059	1.75	5H
Optimized bimorph[g]	520	123	12	2.730	2.36	5H
Maximum strain energy density for bulk free plate[h]				4.0	2.5	5H

[a] Peak-to-peak.
[b] Maximum drive field.
[c] Either PZT-5H or PZT-5A.
[d] Piezo Systems (http://www.piezo.com).
[e] Mide QuickPack actuators (http://www.mide.com/quickpack/qp_pricelist.html).
[f] THin layer UNimorph DrivER and sensor from Face Thunder (from empirical measurements and http://www.face-int.com/thunder/thunder.htm).
[g] Strain-optimized bimorph micro-actuators described in this work.
[h] For d_{31} actuation.

to the field applied to the bimorphs in question ($>2\,\mathrm{V\mu m^{-1}}$ as will be discussed in Section 4). There are four key factors that can limit the magnitude of field applied to piezoelectric actuators: mechanical failure (fracture), electrical failure (dielectric breakdown), depolarization, or saturation of the piezoelectric effect. Bimorphs connected in series or parallel to the drive source are limited by depolarization (as is the case with the first two actuators in Table 1). Unimorphs are not subject to depoling so long as the field is unipolar in the poling direction, or a small magnitude bipolar field. The THUNDER actuators in Table 1 are unimorphs and the field limit listed is based upon commercial specifications. The actuators described here are limited by breakdown and mechanical failure; little saturation has been observed before either electrical or mechanical failure. It is important to note that it is not only the driving method that allows these actuators to be driven at such high fields. The intrinsic and extrinsic geometry modifications give the capability to run the actuator at fields which would fracture traditional rectangular bimorphs. All peak field data for commercially available actuators shown in Table 1 are directly quoted from the manufacturer.

2. Laminate plate theory for the design of multilayer bending actuators

Throughout the following discussion a number of assumptions are made. First, the piezoelectric materials are assumed to be transversely isotropic, that is $d_{31} = d_{32}$ and there are no piezoelectrically induced shearing forces, $d_{36} = 0$ [7]. In general this is only true for the case of polycrystalline piezoelectric materials; with single crystal materials the piezoelectric constant will vary with the orientation relative to the crystal directions. However, if the crystal is cut properly so that the crystal planes are aligned to the actuator geometry, then the material is piezoelectrically orthotropic and this assumption holds for the single crystal case as well. Second, there is no external axial loading, only transverse loading which is applied at the distal end of the actuator. Third, the bonding between each layer is assumed to be perfect, that is, there are no shear strains between layers. Fourthly, for thermal calculations, there is no gradient in temperature through the thickness of any lamina. Also, electrostriction and higher order effects are ignored. The change in effective field due to electromechanical coupling (as in [15]) is also ignored. Finally, when the actuator width is much greater than the thickness, a plane strain state is incurred where $\epsilon_y \equiv 0$ [18]. This causes the Young's modulus and piezoelectric properties to be modified as follows:

$$E_i \rightarrow E_i(1-\nu_i^2)^{-1}, \qquad d_{31} \rightarrow d_{31}(1+\nu_i) \tag{3}$$

Fig. 2 shows the cross-section of a laminate consisting of an arbitrary lamina layup. This will be used to define the lamina geometry throughout this section. The strain in any layer is

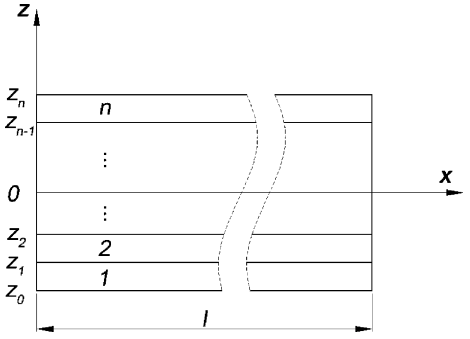

Fig. 2. Actuator layup for arbitrary lamina materials and ply angles.

given by the following:

$$\epsilon_1 = \frac{1}{E}\sigma_1 + d_{31}E_3 p + \alpha_1 \Delta T \tag{4}$$

where σ is an applied stress, E_3 the electric field, α the coefficient of thermal expansion (CTE), and ΔT the change in temperature, which for this application is the change from the cure temperature to room temperature (curing details are given in Section 3). The p term in (4) is a placeholder which is defined as follows:

$$p = \begin{cases} 1 & \text{field parallel to piezoelectric poling} \\ -1 & \text{field antiparallel to piezoelectric poling} \\ 0 & \text{else} \end{cases} \tag{5}$$

Thus, this model can be applied to any combination of piezoelectric and passive plates. Note that for the case of an anisotropic composite material, the strains in (4) are along the fiber direction, as is defined in Fig. 3. More generally, the in-plain strains assume the following form:

$$\begin{bmatrix} \epsilon_1 \\ \epsilon_2 \\ \gamma_{12} \end{bmatrix}_n = \begin{bmatrix} S_{11} & S_{12} & 0 \\ S_{12} & S_{22} & 0 \\ 0 & 0 & S_{66} \end{bmatrix}_n \begin{bmatrix} \sigma_1 \\ \sigma_2 \\ \tau_{12} \end{bmatrix}_n + \begin{bmatrix} d_{31} \\ d_{32} \\ 0 \end{bmatrix}_n E_3^n + \begin{bmatrix} \alpha_1 \\ \alpha_2 \\ 0 \end{bmatrix}_n \Delta T \tag{6}$$

The $[S_{ij}]_n$ terms are the compliances of the nth layer. Solving (6) for the stresses in the piezo layer yields the following:

$$\begin{bmatrix} \sigma_1 \\ \sigma_2 \\ \tau_{12} \end{bmatrix}_n = \begin{bmatrix} Q_{11} & Q_{12} & 0 \\ Q_{12} & Q_{22} & 0 \\ 0 & 0 & Q_{66} \end{bmatrix}_n \left(\begin{bmatrix} \epsilon_1 \\ \epsilon_2 \\ \gamma_{12} \end{bmatrix}_n - \begin{bmatrix} d_{31} \\ d_{32} \\ 0 \end{bmatrix}_n E_3^n - \begin{bmatrix} \alpha_1 \\ \alpha_2 \\ 0 \end{bmatrix}_n \Delta T \right) \tag{7}$$

In Eqs. (6) and (7), the $[Q_{ij}]_n$ terms are the plane strain modified material constants of the lamina as given in Table 2.

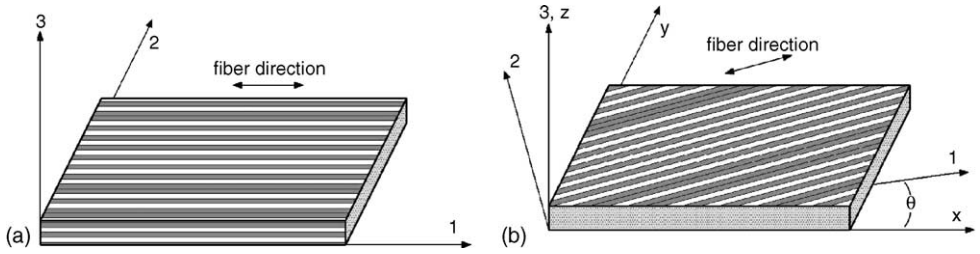

Fig. 3. Lamina axes diagram for (a) plate aligned to global axes and (b) arbitrary orientation.

To generalize this to arbitrary lamina orientations, the following notation is used:

$$\begin{bmatrix}\sigma_x\\ \sigma_y\\ \tau_{xy}\end{bmatrix}_n = \begin{bmatrix}\bar{Q}_{11} & \bar{Q}_{12} & \bar{Q}_{16}\\ \bar{Q}_{12} & \bar{Q}_{22} & \bar{Q}_{26}\\ \bar{Q}_{16} & \bar{Q}_{26} & \bar{Q}_{66}\end{bmatrix}_n \left(\begin{bmatrix}\epsilon_x\\ \epsilon_y\\ \gamma_{xy}\end{bmatrix}_n - \begin{bmatrix}d_{31}\\ d_{32}\\ 0\end{bmatrix}_n E_3^n - \begin{bmatrix}\bar{\alpha}_x\\ \bar{\alpha}_y\\ \bar{\alpha}_{xy}\end{bmatrix}_n \Delta T \right) \tag{8}$$

Where the new $[\bar{Q}_{ij}]_n$ is the adjusted stiffness matrix whose elements have the following properties:

$$[\bar{Q}_{ij}] = [T]^{-1}[Q_{ij}][T]^{-T} \tag{9}$$

and the transformed CTE terms $[\bar{\alpha}_i]$ are as follows:

$$[\bar{\alpha}] = [T]^{-1}[\alpha] \tag{10}$$

where the transformation matrix $[T]$ is defined in (11).

$$[T] = \begin{bmatrix} m^2 & n^2 & 2mn\\ n^2 & m^2 & -2mn\\ -mn & mn & m^2-n^2\end{bmatrix} \tag{11}$$

In (11), the terms m and n are cos(θ) and sin(θ) respectively where θ is the angle between the global axes and the lamina fiber direction (see Fig. 3(b)). Now the forces and moments (per unit width) are given as a function of the ply stresses:

$$[N_i] = \sum_n \int_{z_{n-1}}^{z_n} [\sigma_i]_n \, \mathrm{d}z,$$

$$[M_i] = \sum_n \int_{z_{n-1}}^{z_n} [\sigma_i]_n z \, \mathrm{d}z \tag{12}$$

Next, the actuator properties are determined as a function of the ply layup using laminate plate theory. First, the relationship between the midplane strains and curvatures and the forces and moments is given by:

$$\begin{bmatrix}N\\ M\end{bmatrix} = \begin{bmatrix}A_{ij} & B_{ij}\\ B_{ij} & D_{ij}\end{bmatrix}\begin{bmatrix}\epsilon^0\\ \kappa\end{bmatrix} \tag{13}$$

In Eq. (13) the A, B, and D terms are given as follows:

$$A_{ij} = \sum_n [\bar{Q}_{ij}]_n (z_n - z_{n-1}),$$

$$B_{ij} = \frac{1}{2}\sum_n [\bar{Q}_{ij}]_n (z_n^2 - z_{n-1}^2),$$

$$D_{ij} = \frac{1}{3}\sum_n [\bar{Q}_{ij}]_n (z_n^3 - z_{n-1}^3) \tag{14}$$

In Eq. (14), the term z_n is the directed height of the nth lamina with respect to the mid plane as is shown in Fig. 2. In Eq. (13), the total forces and moments per unit width $[\,N\;\;M\,]^{\mathrm{T}}$ can be split up into three terms: the externally applied moments and the internal forces and moments from the piezoelectric effect and thermal expansion all per unit width.

$$\begin{bmatrix}N\\ M\end{bmatrix} = \begin{bmatrix}N_{\mathrm{ext}}\\ M_{\mathrm{ext}}\end{bmatrix} + \begin{bmatrix}N^p\\ M^p\end{bmatrix} + \begin{bmatrix}N^t\\ M^t\end{bmatrix} \tag{15}$$

The piezoelectric forces and moments are defined as follows:

$$[N_i(E_3)]^p = \sum_n \int_{z_{n-1}}^{z_n} [\bar{Q}_{ij}]_n d_{3j} E_3 \; p \, \mathrm{d}z,$$

$$[M_i(E_3)]^p = \sum_n \int_{z_{n-1}}^{z_n} [\bar{Q}_{ij}]_n d_{3j} E_3 z \; p \, \mathrm{d}z \tag{16}$$

Table 2
Design parameters for actuator materials

Parameters	UHM CF[a]	S2Glass[a]	Steel	Si	PZT-5H	PZN-PT	Units
E_1	350	60	193	190	62	15	GPa
E_2	7	7	193	190	62	15	GPa
ρ	1500	1600	7800	2300	7800	8300	kg m^{-3}
d_{31}	–	–	–	–	−320	−950	pmV^{-1}
$\sigma_{u,1}$[b]	840	1400	900[c]	120	200[d]	40[d]	MPa

[a] Cured.
[b] Ultimate stress.
[c] Yield stress.
[d] Estimated from empirical observations.

Similarly, the thermal expansion forces and moments are:

$$[N_i]^t = \sum_n \int_{z_{n-1}}^{z_n} [\bar{Q}_{ij}]_n [\bar{\alpha}_j]_n \Delta T \, \mathrm{d}z,$$

$$[M_i]^t = \sum_n \int_{z_{n-1}}^{z_n} [\bar{Q}_{ij}]_n [\bar{\alpha}_j]_n \Delta T z \, \mathrm{d}z \tag{17}$$

Solving Eq. (13) for the midplane strains and curvatures yields the following:

$$\begin{bmatrix} \epsilon^0 \\ \kappa \end{bmatrix} = \begin{bmatrix} A_{ij} & B_{ij} \\ B_{ij} & D_{ij} \end{bmatrix}^{-1} \left(\begin{bmatrix} N_{\text{ext}} \\ M_{\text{ext}} \end{bmatrix} + \begin{bmatrix} N^p \\ M^p \end{bmatrix} + \begin{bmatrix} N^t \\ M^t \end{bmatrix} \right) \tag{18}$$

Finally, the free displacement and blocked force of the actuator are found as a function of the applied fields ($[E_3]_n$) and the external loading. Since axial strains do not contribute to lateral displacement of the distal end of the cantilever, the only quantity of interest from Eq. (18) is κ_x. First note that the curvature κ_x is related to the displacement as $\mathrm{d}^2\delta(x)/\mathrm{d}x^2 = \kappa_x$ where $\delta(x)$ is the displacement of the actuator at any point along the x-axis and define:

$$C = \begin{bmatrix} A_{ij} & B_{ij} \\ B_{ij} & D_{ij} \end{bmatrix}^{-1} \tag{19}$$

Next the external forces and moments are included into Eq. (18). Note that for a clamped-free cantilever with no external axial forces and an external moment about the y-axis, $[\, N_{\text{ext}} \;\; M_{\text{ext}} \,]^{\mathrm{T}} = [\, 0 \; 0 \; 0 \;\; M_x(x) \;\; 0 \; 0 \,]^{\mathrm{T}}$. For convenience, define the following:

$$P(E_3) = C_{41} N_x^p(E_3) + C_{42} N_y^p(E_3) + C_{44} M_x^p(E_3) + C_{45} M_y^p(E_3) \tag{20}$$

where C_{ij} is the (i, j)th element of C ($i, j \in \{1:6\}$). Thus it can be seen that the curvature is related to the internal and external moments as follows (ignoring the static thermal forces and moments):

$$\frac{\mathrm{d}^2\delta(x)}{\mathrm{d}x^2} = P(E_3) + C_{44} M_x(x) \tag{21}$$

A functional diagram of the actuator with respect to the external parameters in Eq. (21) is shown in Fig. 4.

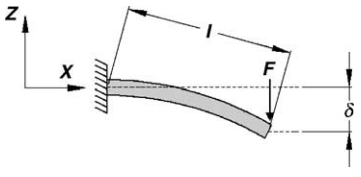

Fig. 4. Actuator diagram with respect to external parameters.

2.1. Actuator geometry

For the case of transverse external loading, significant tensile stresses will be developed in the outer layers. For the case of a clamped-free cantilever, the moment per unit width generated in the beam is $M_x(x) = -F(l-x)/w$. For a constant cross-section, this moment is proportional to the stress at a given point x, thus the stresses will be maximum at the proximal end of the actuator. If the cross-section varies along x, the stress profile can be controlled and large stresses can be eliminated. Varying the thickness of the piezoelectric material is not practical given the thickness of the commercially available PZT plates used (127 μm); however, controlling the width is relatively simple. To explore this further, consider Eq. (21) and expand the external moment.

$$\frac{\mathrm{d}^2\delta(x)}{\mathrm{d}x^2} = P(E_3) - \frac{C_{44} F(l-x)}{w(x)} \tag{22}$$

Thus the free deflection (with $F \equiv 0$) does not vary with a change in the width profile. Next it is necessary to determine $w(x)$ explicitly for each profile for use in Eq. (22). For the case of a trapezoidal profile, this is given by the following:

$$w(x) = w_{\text{nom}} \left(\frac{2(1-w_r)}{l} x + w_r \right) \tag{23}$$

For the above equation, w_{nom} is the nominal width (the width at $x = l/2$) which is the same for all trapezoidal width profiles (to keep the platform area and thus the mass constant for collateral comparisons) and the width ratio, $w_r = w_0/w_{\text{nom}}$. Example width profiles are shown in Fig. 5. In Fig. 5 w_0 and w_l are the width at the proximal and distal ends respectively. It is trivial to see that for a thin long clamped-free beam, point loaded at the distal end, the strain at the proximal end is inversely proportional to the width ratio. To illustrate this point more concisely the normalized strain profile along the length of the actuator is plotted for a few width ratios in Fig. 6(a). Thus it is clear that altering the width can lower peak stresses, increasing the load to fracture; now it will be shown that for a fixed actuator area, varying the width can increase or decrease the blocked force. Again the curvature is given by:

$$\frac{\mathrm{d}^2\delta(x)}{\mathrm{d}x^2} = P(E_3) - \frac{C_{44} F}{w_{\text{nom}}} \left[\frac{l-x}{(2(1-w_r)/l)x + w_r} \right] \tag{24}$$

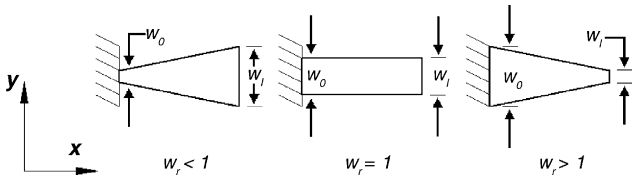

Fig. 5. Three representative width profiles.

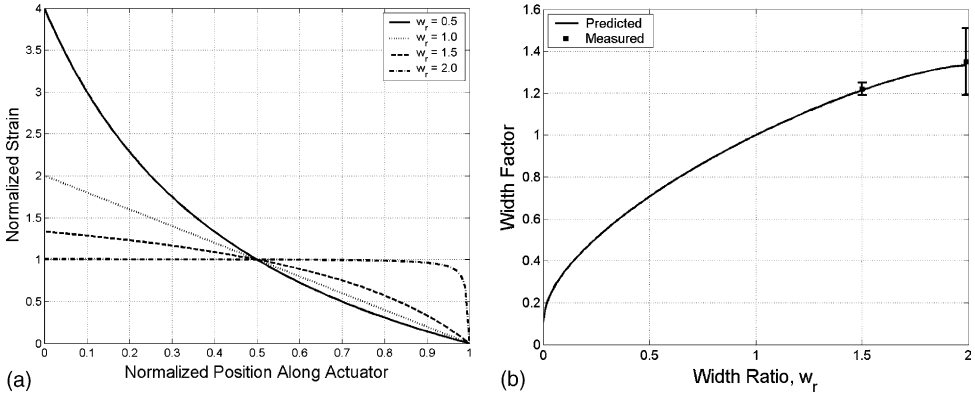

Fig. 6. Strain profiles for a few width ratios (a) and width factor as a function of width ratio (b) with experimental data ($N = 3$) for two geometries.

Integrating this twice noting the strict boundary conditions yields the displacement at the distal end of the actuator:

$$\delta(l) = \frac{P(E_3)l^2}{2} - \frac{C_{44}Fl^3}{w_{\text{nom}}} \times \left[\frac{(w_r-2)^2\ln\left((2-w_r)/w_r\right) - 6 + 10w_r - 4w_r^2}{8(1-w_r)^3}\right] \tag{25}$$

Now when $\delta(l) = 0$, the blocked force, F_{b}, is defined as:

$$F_{\text{b}} = \frac{3P(E_3)w_{\text{nom}}}{2C_{44}l}W(w_r) \tag{26}$$

where W is the width factor is given by the following:

$$W(w_r) = \frac{8(1-w_r)^3}{3(w_r-2)^2\ln((2-w_r)/w_r) - 18 + 30w_r - 12w_r^2} \tag{27}$$

The width factor is plotted in Fig. 6(b), showing the variation with the width ratio. Note that for $w_r = 1$, $W = 1$, yielding the same blocked force prediction as for the rectangular case. Substituting the blocked force and free displacement into Eq. (1) will yield the mechanical energy:

$$U_m = \frac{3P(E_3)^2w_{\text{nom}}l}{8C_{44}}W(w_r) \tag{28}$$

Note that the term $w_{\text{nom}}l$ represents the area of the actuator, and that the energy is linear with the area. Thus the greatest energy and energy densities are obtained from a width ratio of 2, which represents a triangular actuator.

2.2. Rigid extension

Another method of improving the energy density of a cantilever bending actuator is to add an extension to the distal end. The concept of a rigid extension was introduced by Campolo et al. [3] and is shown in Fig. 7. This extension acts as a lever which converts the force on the tip to a force and moment at the interface between the piezo and the extension as in Eq. (29). By transforming the point load to a force and moment as seen by the active material, the strain is more uniformly distributed along the length. Because of this, large differences in stress between different sections are decreased and each infinitesimal section of the piezoelectric material can be driven closer to the fracture strain. Thus the extension does not add mechanical energy to the system, but instead allows all parts of the actuator to contribute more uniformly to the work. To examine the effects of the extension, first the external moment term, $M_x(x)$ from Eq. (21) needs to be determined.

$$\begin{bmatrix} F \\ M_{\text{ext}} \end{bmatrix} = \begin{bmatrix} 1 \\ -l_{\text{ext}} \end{bmatrix} F_{\text{ext}} \tag{29}$$

Now it is clear that there will be a superposition of a pure moment and a force generated by the point load. Thus the moment per unit width is given by the following:

$$M_x(x) = -\frac{F_{\text{ext}}((l + l_{\text{ext}}) - x)}{w_{\text{nom}}} \tag{30}$$

where now $F_{\text{ext}} = F$ applied at the tip of the extension. Note that in the above equation, the width is set to be constant and equal to w_{nom}. Next, the curvature in Eq. (21) is split into two terms, one from the internal piezoelectric moment ($\mathrm{d}^2\delta_p(x)/\mathrm{d}x^2$) and one from the externally applied moment ($\mathrm{d}^2\delta_f(x)/\mathrm{d}x^2$). At $x = l$, the displacement at the interface between the piezo and extension is found by integrating twice these two curvatures:

$$\delta_p(l) = \frac{P(E_3)l^2}{2} \tag{31}$$

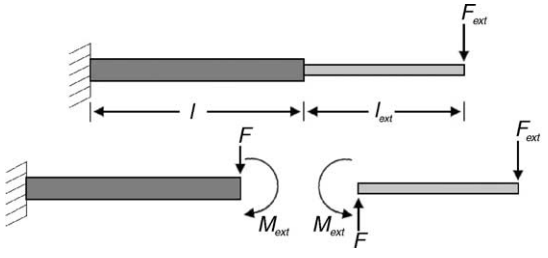

Fig. 7. Exploded image of actuator with extension.

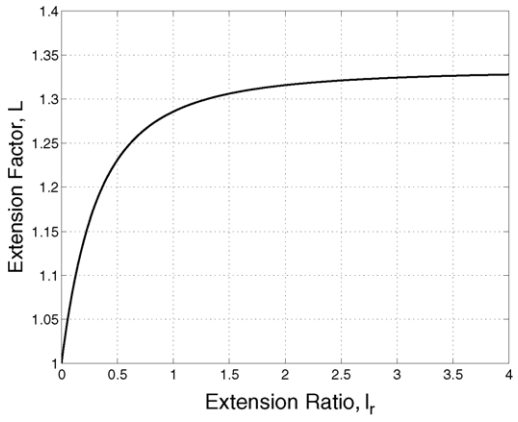

Fig. 8. Energy improvement as a function of the extension ratio.

$$\delta_f(l) = -\frac{C_{44}F_{\text{ext}}}{w_{\text{nom}}}\left(\frac{l^3}{3} + \frac{l_{\text{ext}}l^2}{2}\right) \tag{32}$$

Next note that the displacement at the distal end of the extension is a function of the displacement at the interface, the slope at the interface, and the extension length.

$$\delta(l + l_{\text{ext}}) = \delta(l) + \left.\frac{\mathrm{d}\delta(x)}{\mathrm{d}x}\right|_{x=l} l_{\text{ext}} \tag{33}$$

Adjusting the displacement terms in (31) and (32) for the extension and simplifying by introducing the length ratio, l_r, defined as the ratio of the extension length to the actuator length (without the extension), yields two displacement terms:

$$\delta_p(l + l_{\text{ext}}) = \frac{Pl^2}{2}(1 + 2l_r) \tag{34}$$

$$\delta_f(l + l_{\text{ext}}) = -\frac{C_{44}F_{\text{ext}}l^3}{3w_{\text{nom}}}(1 + 3l_r + 3l_r^2) \tag{35}$$

To solve for the blocked force at the extension, the superposition of the two displacements must be zero, i.e. $\delta_p(l + l_{\text{ext}}) + \delta_p(l + l_{\text{ext}}) = 0$. Using this and solving for F_{ext} yields the blocked force as follows:

$$F_{\text{b,ext}} = \frac{3P(E_3)w_{\text{nom}}}{2C_{44}l}\frac{(1 + 2l_r)}{(1 + 3l_r + 3l_r^2)} \tag{36}$$

Note that this is done without regard to the width profile, and setting the width to w_{nom}. Now the energy of the actuator with the extension is given as follows by substituting the terms in (36) and the free displacement from (34) into (1):

$$U_{m,\text{ext}} = \frac{3P(E_3)^2 l w_{\text{nom}}}{8C_{44}}L(l_r) \tag{37}$$

The term L in the above equation is a unitless function of the extension ratio:

$$L(l_r) = \frac{(1 + 2l_r)^2}{(1 + 3l_r + 3l_r^2)} \tag{38}$$

Finally, assume that the extension adds negligible mass to the actuator, and thus the energy and energy density are proportional to L. The function L is plotted in Fig. 8 as a function of the extension ratio l_r.

Note that if $l_r = 0$, Eq. (37) reduces to the same energy as for the rectangular case with no extension. To determine the maximum improvement in energy, observe that $\lim_{l_r\to\infty} L = 4/3$. Thus the maximum improvement in energy and energy density is 4/3. Note that for all the equations in Section 2.2, the extension is assumed to be perfectly rigid, or more practically to have a stiffness >10× that of the actuator without the extension (Figs. 9 and 10).

2.3. Complete model

Combining the results from Sections 2.1 and 2.2 yields the complete description of the actuator performance. This is done by again performing the integrations on the curvature, but now combining the width and extension terms in the external moment.

$$M_x(x) = -\frac{F_{\text{ext}}(l(1 + l_r) - x)}{w_{\text{nom}}((2(1 - w_r)/l)x + w_r)} \tag{39}$$

The remainder of the procedure is identical to that of Section 2.2. First, the displacement due to the applied electric

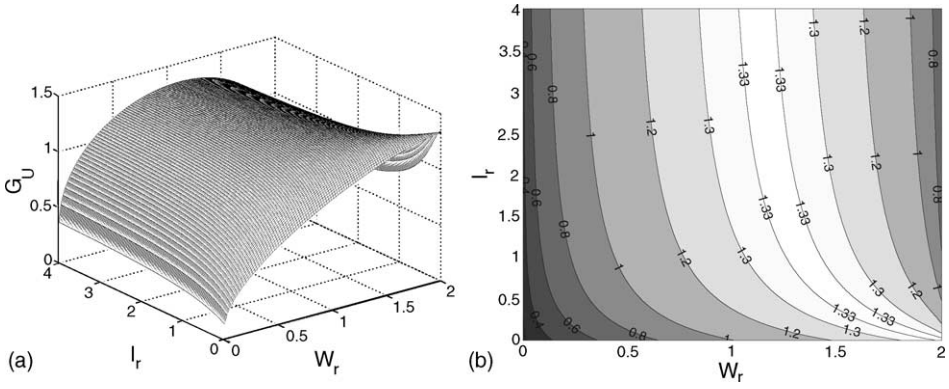

Fig. 9. Energy improvement as a function of the geometry: (a) 3D plot of G_U and (b) contour plot of the same function.

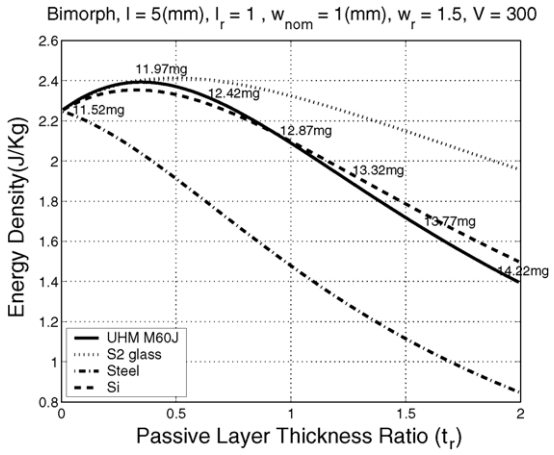

Fig. 10. Predicted effect of passive layer thickness on energy density for a bimorph.

field is found, along with the displacement due to an external force. These are then added and set to zero to find the blocked force. Note that the free displacement is identical to the results in Section 2.2. First, integrating twice to find the displacement from an external force yields the following:

$$\delta_f(l) = -\frac{C_{44}F_{\text{ext}}l^3}{3w_{\text{nom}}}G_l(w_r, l_r) \tag{40}$$

The term G_l is a function of the width ratio and extension ratio $G_l(w_r, l_r) = (g_a + g_b)/g_c$ where the g_i terms are defined as follows:

$$g_a = 6(w_r - 1)(-3 - 2l_r + 2w_r + 2l_r w_r),$$

$$g_b = 3(w_r - 2)(-2 - 2l_r + w_r + 2l_r w_r)\ln\left(\frac{2 - w_r}{w_r}\right),$$

$$g_c = 8(1 - w_r)^3 \tag{41}$$

Recall again Eq. (33) for a rigid extension and substitute this into (40) yielding the following:

$$\delta_f(l + l_{\text{ext}}) = -\frac{C_{44}F_{\text{ext}}l^3}{3w_{\text{nom}}}G_{l_{\text{ext}}}(w_r, l_r) \tag{42}$$

where the parameter $G_{l_{\text{ext}}}(w_r, l_r) = (g_d + g_e)/g_c$ and the g_i terms are defined as follows:

$$g_d = 6(w_r - 1)(3 + 4l_r - 2w_r - 4l_r w_r),$$

$$g_e = 3(-2 - 2l_r + w_r + 2l_r w_r)^2 \ln\left(\frac{2 - w_r}{w_r}\right) \tag{43}$$

Now adding Eqs. (35) and (42) and setting this to zero yields the blocked force:

$$F_{\text{b,ext}} = \frac{3P(E_3)w_{\text{nom}}}{2C_{44}l}G_{F_{\text{b}}}(w_r, l_r) \tag{44}$$

where the term $G_{F_{\text{b}}}$ is called the blocked force geometry constant and is defined as follows:

$$G_{F_{\text{b}}}(w_r, l_r) = \frac{(1 + 2l_r)}{G_{l_{\text{ext}}}(w_r, l_r)} \tag{45}$$

For convenience, call the term $(1 + 2l_r)$ in (35) G_δ, the free displacement geometry constant. Lastly, call G_U the product $G_\delta G_{F_{\text{b}}}$; thus the mechanical energy can be written as a function of G_U:

$$U_m = \frac{3P(E_3)^2 l w_{\text{nom}}}{8C_{44}}G_U(w_r, l_r) \tag{46}$$

Thus G_U multiplies with the energy and also the energy density, therefore G_U is a relative measure of the geometrically improved energy density. Finally, the energy density is given as:

$$D_U = \frac{3P(E_3)^2/8C_{44}}{\sum_n \rho_n t_n}G_U(w_r, l_r) \tag{47}$$

where ρ_n and t_n are the densities and thicknesses of the nth layer respectively. The G_U parameter is plotted below as a function of the width and extension ratios. This completes the model for cantilever piezoelectric bending actuators including any number, anisotropy, or orientation of the constituent layers, number, placement, or makeup of piezoelectric layers, and overall geometry.

3. Fabrication

From the design analysis, ultra-high modulus (UHM) unidirectional carbon fiber composites are chosen for the passive layers, similar to [24]. Carbon fiber-based composites have the added benefit of being decent ($\approx 1 \times 10^{-3}\,\Omega\,\text{cm}$) electrical conductors (for low current applications), thus no additional electrodes need to be implanted within the actuator layup. Ideally, such UHM materials would be used to create the rigid extension. However, because of concerns for shorting the piezo electrodes, non-conductive fiber glass layers are used. Since extension compliance is a significant concern the highest modulus glass material, unidirectional S2Glass, is layered to stiffen the extension. Each layer is laser-micromachined into desired shapes using a computer controlled precision pulsed laser (QuickLaze from New Wave Research Inc.) to control dimensions and relative ply angles. The composite material matrices are thermoset polymers initially in a catalyzed uncured state (called prepreg) and are cut in this state. After all materials are cut, the layers are assembled with the desired layup and cured in a vacuum oven. The bonding between each layer is achieved by the flow of the composite matrix epoxy while curing. Thus, the actuator requires neither electrodes nor additional bonding layers.

To determine the geometric parameters for the desired application, the effects of the various constituent parameters in Section 2.3 on the output performance is determined. First, the width ratio and the length ratio are maximized to the highest practical degree. For practical applications, the width ratio will not reach the maximum value of 2 since a distal end with zero width results in too fragile a structure, and the connection to the extension needs to be as rigid as possible. The length ratio cannot be increased indefinitely since the

extension mass becomes a concern. The current design uses a width ratio of 1.5 and an extension ratio of 1.

In choosing the geometry of the actuator, three output parameters are used: the displacement, the blocked force, and the energy density. From the results in Section 2.3, the following is clear:

$$D_U = g_1(t_r), \qquad \delta = g_2(t_r, l),$$
$$F_\mathrm{b} = g_3(t_r, l, w_\mathrm{nom}) \tag{48}$$

where l and w_nom are again the actuator length and nominal width respectively and t_r the ratio of the passive layer thickness to a single piezoelectric plate thickness. First, for given constituent layer mechanical and piezoelectric properties, the energy density is maximized over the passive layer thickness. From this plot it can be seen that the maximum energy density occurs at a thickness ratio of approximately 0.35 for the bimorph with respect to the given material properties and using unidirectional UHM composites. Note that the UHM energy density is plotted alongside similar curves for other common engineering materials for comparison reasons. Now the remaining two parameters, the displacement and blocked force, have two unknowns, the length and the nominal width. Solving these two equations for application specific displacement and blocked force yields the length and width parameters. The properties of the various engineering materials considered for the passive and active layers are given in Table 2.

3.1. Piezoelectric material choice

One of the best criterion for choice of piezoelectric material is the strain energy density. The strain energy density is defined as follows:

$$e_\mathrm{max} = \frac{1}{\rho}\left(\frac{1}{2}E\epsilon_\mathrm{max}^2\right) \tag{49}$$

where e_max is the maximum strain energy density, ρ the density, E the Young's modulus, and ϵ_max the maximum strain. This last term, ϵ_max, can be thought of as derived from one of two different elastic modes: either the strain developed from external loading, or the induced piezoelectric strain at a given field, namely $d_{ij}E_i$. Two piezoelectric materials are considered: PZT-5H, a soft polycrystalline ceramic, and PZN-PT, a ferroelectric relaxor-based single crystal [10,23]. The former has the benefits of low cost, ease of availability, and relatively high elastic modulus while the latter has a much larger piezoelectric coupling coefficient with the drawbacks of cost, availability, and poor fracture properties. The properties of both materials are given in Table 2. To determine which strain to use in (49), choose $\min(d_{31}E_3, \epsilon_f)$, where ϵ_f is the mechanical fracture strain. Thus, because of the extremely low fracture toughness associated with single crystal materials, PZT shows a factor of two better performance. Therefore, polycrystalline piezoelectric materials are used throughout the following discussion.

3.2. Utilizing thermal expansion mismatches

Before curing, the materials in the actuator are free, and when brought up to high temperatures for curing, they freely expand or contract depending upon the sign of their CTE. The state before any significant cross linking of the matrix epoxy occurs is referred to as the stress free state. Once bonding occurs, the materials are joined at the interface. By designing the elastic layer to have a proper CTE with respect to the piezoelectric layer, a tailored stress is applied to the piezoelectric material after the actuator is subsequently brought down to room temperature. Quantitatively, the thermal stresses developed in each layer of the laminate can be determined by examining Eq. (18). By solving (18) for the midplane strains and curvatures and noting that the strain in the ith layer is related to these two terms via Eq. (50), the stresses and strains can be predicted on a ply by ply basis.

$$\epsilon_i = \epsilon^0 + \kappa z_i \tag{50}$$

Section 4.1 provides a diagram of the strains in the various layers of the bimorph actuator.

4. Driving techniques

There are a number of traditional methods for applying a field to bimorph piezoelectric bending actuators. The first two methods require only a single source which is connected electrically in parallel or series with the electrodes of the bimorph as described by Wang et al. [17] and are shown in Fig. 11(a). For the series case, the field is applied across the two electrodes and the polarization of each piezoelectric layer is opposite. Thus the application of the electric field creates opposing strains in the two layers. For the case of the parallel configuration, the center electrode is grounded, while a positive voltage is applied to the outer two electrodes of similarly poled piezoelectric layers. Thus, instead of opposite polarizations, the field orientation creates opposite strains. The major differences between these two methods are that the series configuration will require twice the voltage to ob-

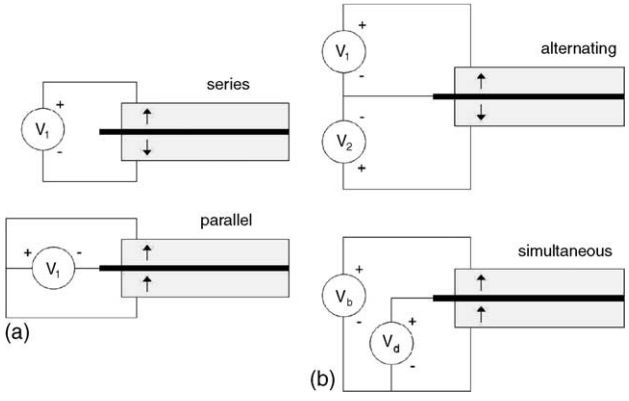

Fig. 11. Drive diagram for (a) single source and (b) dual source.

tain the same field, while the parallel method requires one additional connection. The overall problem with these two methods lies in the limit of the field that could be applied before depoling occurs within the layer that is poled antiparallel to the field direction. For PZT at room temperature, this is approximately 0.5 $V\mu m^{-1}$, however the desired field (which will draw the constituent actuator materials close to fracture) is approximately 2–3$V\mu m^{-1}$ which would depole one of the layers, making the actuator useless. This effect is amplified as the operating temperature approaches the Curie temperature or in the presence of applied mechanical stresses. It is clear that in order to obtain the highest possible performance, each piezoelectric layer must be kept under positive field with respect to its polarization direction. Thus the achievable energy density would be much too low for either of these techniques (as can be seen in Table 1).

The dual source drive schematics are shown in Fig. 11(b). The first of these two is termed the alternating drive where the dual source drive either layer independently. Each source is kept 180° out of phase with the other, each driven unipolar. This keeps each layer driven only in a positive sense, however requires two independent sources for each actuator, and thus a total of $2n + 1$ wires and $2n$ sources for n actuators. The second option, termed the simultaneous drive, instead biases the entire actuator. Thus the bias and ground can be common for multiple actuators, requiring $n + 2$ wires and $n + 1$ sources for n actuators.

4.1. Results

The mechanical energy provided by these two competing drive methods was measured by individually measuring the displacement and blocked force using custom built optical [2] and strain [19] sensors respectively. First, each driving method is evaluated based upon the static performance with no applied load. The results show that the alternating method exhibits greater saturation, while providing approximately 5% less displacement than the simultaneous drive for a given maximum field. Under cyclic actuation however, the simultaneous drive shows slightly greater hysteresis. These three differences can be seen by a comparison of the output traces in Fig. 12. Since for the simultaneous case the relative magnitudes of the bias field and maximum drive field are variable, an attempt was made to compensate for this hysteresis increase by increasing the relative magnitude of the bias field. The idea is that the added hysteresis originates from stress depolarization of the piezoelectric plate which is experiencing relatively less field magnitude during any given half stroke. The field at this point is less than is required to maintain polarization while under high stresses. The results of this test, as shown in Fig. 12, display that this principle of reducing the hysteresis does work, however the displacement amplitude decreases significantly. Next, the linearity and hysteresis in blocked force was examined using a custom built load cell [19]. This was done first by incrementally applying a field to a bimorph, optically zeroing the actuator displacement with

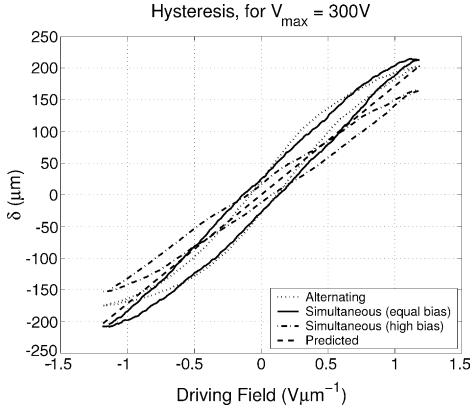

Fig. 12. Comparison of hysteresis plots for all three dual source driving methods (drive voltage is with respect to $V_{max}/2$).

the load cell, and measuring the resulting force. This gives a very linear curve for the blocked force as a function of field as is shown in Fig. 13(a). To quantify the hysteresis in the applied force, the load cell was put in contact with the free end of the actuator and the bimorph was driven from $V_d = 0$ to V_{max} where $V_{max} = V_b$ for incrementally increased bias fields. The results are shown in Fig. 13(b). It is well understood that piezoelectric materials undergo a softening at higher fields. This softening will be apparent when observing the Q and resonant frequencies as a function of the applied field. As an example of this effect, the frequency response of an unloaded bimorph was determined for iteratively increased field magnitudes. Since the actuator alone is a high Q system, this could not be tested up to the field magnitudes that will be experienced when connected to a load. From the frequency response seen in Fig. 14(a), the resonant frequency and Q can be extracted as a function of the field magnitude. Note that the actuator is driven in simultaneous mode with $V_{max} = V_b$. The results are shown in Fig. 14(b). Finally, the performance of the bimorph actuators described here are given in Table 3. Note that in Table 3 there are two known causes of the difference between the predicted and experimental performance values. The first is due to stress based d_{31} enhancements. It is known that the piezoelectric coupling coefficients of polycrystalline piezoceramics is increased with applied tensile stress and decreased with compressive stress [1,8,22]. For the case of the bimorphs described here, the piezoelectric plate performing work is always in tension (either imposed elastically from the opposite plate or from an external reaction force) and will increase both peak displacement and blocked force. The second cause for the discrepancy is piezoceramic softening under high drive fields (as is displayed in the decrease in resonant frequency shown in Fig. 14(a)). This softening will result in an increase in displacement and a decrease in blocked force. Corrections for these effects will not be presented here, other than noting that altering d_{31} and the elastic modulus values as a function of applied field causes the predicted and measured performance to be nearly identical.

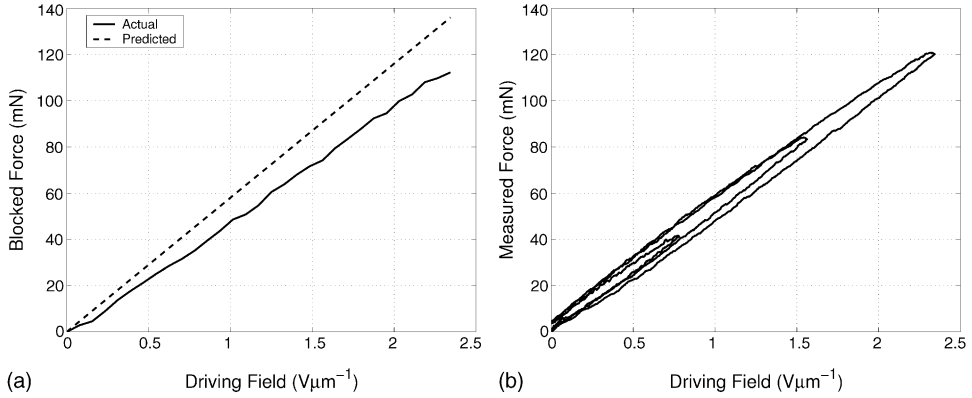

Fig. 13. Blocked force with the drive field (a) and force transducer measurements from bimorph showing hysteresis (b) both using the simultaneous drive method (drive voltage is with respect to V_{max}).

Table 3
Performance results for energy density optimized bimorph piezoelectric bending actuators (for $N = 32$ actuators, simultaneous drive, 2.4 Vμm^{-1})

Parameter	Units	Predicted	Measured	Error (%)
δ[a]	μm	406	520 ± 56.9	+28.1
F_b[a]	mN	136	123 ± 20.5	−9.6
m	mg	11.72	11.75 ± 0.8	+2.6
U_m	μJ	28	32 ± 7.1	+14.3
D_U	J kg^{-1}	2.35	2.73 ± 0.5	+16.2

[a] Peak-to-peak.

5. Discussion

At the beginning of this paper, the concept of high energy density actuators was introduced as structures in which all active materials are driven as close as possible to their maximum achievable strain (limited by either saturation, fracture, breakdown, etc.). It is desirable at this point to estimate numerically the strain present in each layer of the actuators due to internal (thermal expansion, piezoelectric displacement) and external (external loads) excitations typically expected for the given application. This is readily accomplished by calculating the midplane strains and curvatures when substituting the internal and external forces and moments into Eq. (18) and then applying this to each layer via Eq. (50). This ease of strain analysis is an ancillary benefit of using laminate plate theory for the design of bending actuators and sensors. The thermal, piezoelectric, external, and total strains (because of the principle of superposition) are shown for the outer surface of the top piezoelectric layer (because of symmetry) in Fig. 15 for a bimorph as well as for the passive layer for an externally applied 100 mN load.

Note that in Fig. 15 the total strain is nearly constant along the length of the actuator and close to the fracture strain of the material, thus ensuring that each element of the piezoelectric material is performing nearly maximal useful work. In summary, there are four techniques described here to improve the energy density of piezoelectric cantilever bending actuators: width tapering, extension, high performance material choice, and high field drive. While the geometric alterations contribute an increase of 33% (Fig. 9), the use of composite materials yields between a maximum of 5–10% improvement (depending upon material choice, Fig. 10) as well as other ancillary benefits. Finally, the dual source simultaneous drive technique coupled with the strain uniformity provided by the geometric modifications provide an increase of approximately a factor of 10. In total, such actuators described here exhibit energy densities on the order of 10–50 times those of commercially available adaptations (Fig. 16).

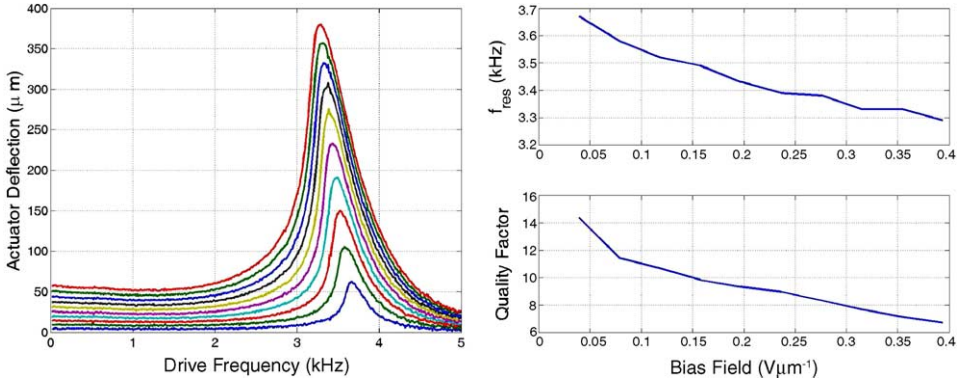

Fig. 14. Bimorph frequency response for varying field magnitudes (a) and the associated resonant frequency and Q (b).

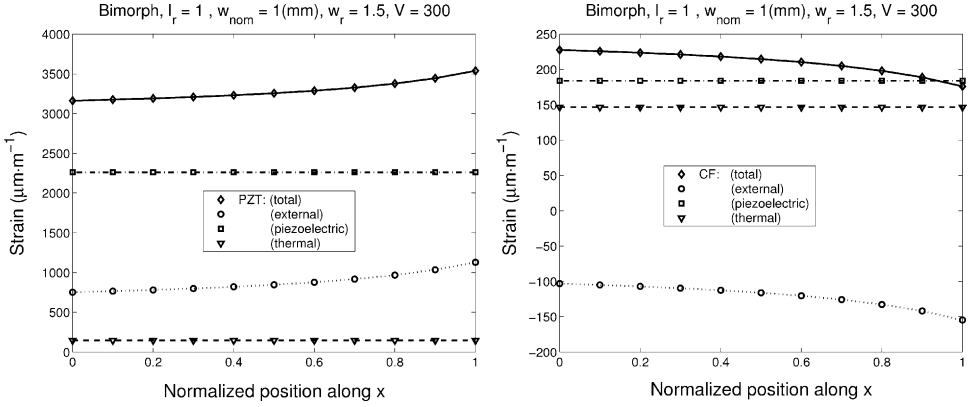

Fig. 15. Strains in the constituent layers of the bimorph actuator (simultaneous drive).

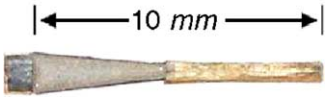

Fig. 16. Completed bimorph actuator.

Acknowledgments

The authors would like to thank Jacoby Hickerson for assistance in actuator construction and Srinath Avadhanula for insightful discussions. This work was supported under funding by ONR MURI N00014-98-1-0671, DARPA and NSF IIS-0083472.

References

[1] M. Algueró, B.L. Cheng, F. Guiu, M.J. Reece, M. Poole, N. Alford, Degradation of the d_{33} piezoelectric coefficient for PZT under static and cyclic compressive loading, J. Eur. Ceram. Soc. 21 (2001) 1437–1440.

[2] S. Avadhanula, R.J. Wood, E. Steltz, J. Yan, R.S. Fearing, Lift force improvements for the micromechanical flying insect, in: Proceedings of the IEEE/RSJ International Conference on Intelligent Robots and Systems, Las Vegas, NV, October 2003.

[3] D. Campolo, R. Sahai, R.S. Fearing, Development of piezoelectric bending actuators with embedded piezoelectric sensors for micromechanical flapping mechanisms, in: Proceedings of the IEEE International Conference on Robotics and Automation, Taipei, Taiwan, September 2003.

[4] D.L. DeVoe, A.P. Pisano, Modeling and optimal design of piezoelectric cantilever microactuators, J. Microelect. Mech. Syst. 6 (3) (1997) 266–270.

[5] M. Gogola, G. Fischer, M. Goldfarb, E. Garcia, The development of two piezoelectrically-actuated mesoscale robot quadrupeds, in: Proceedings of the SPIE Conference on Microrobotics and Microassembly, vol. 3834, Boston, MA, September 1999, pp. 76–84.

[6] W.E. Green, P.Y. Oh, An aerial prototype for situational awareness in closed quarters, in: Proceedings of the IEEE/RSJ International Conference on Intelligent Robots and Systems, Las Vegas, NV, October 2003, pp. 61–66.

[7] H. Kioua, S. Mirza, Piezoelectric induced bending and twisting of laminated composite shallow shells, J. Smart Mater. Struct. 9 (2000) 476–484.

[8] S.W. Meeks, R.W. Timme, Effects of one-dimensional stress on piezoelectric ceramics, J. Appl. Phys. 46 (10) (1975) 4334–4338.

[9] J.-D. Nicoud, J.-C. Zufferey, Towards indoor flying robots, in: Proceedings of the IEEE/RSJ International Conference on Intelligent Robots and Systems, Lausanne, Switzerland, October 2002, pp. 787–792.

[10] S.E. Park, T.R. Shrout, Ultrahigh strains and piezoelectric behavior in relaxor based ferroelectric single crystals, J. Appl. Phys. 82 (4) (1997) 1804–1811.

[11] J. Pasquero, V. Hayward, STReSS: a practical tactile display system with one millimeter spatial resolution and 700 Hz refresh rate, in: Proceedings of the Eurohaptics, 2003, pp. 94–110.

[12] M. Sitti, D. Campolo, J. Yan, R.S. Fearing, T. Su, D. Taylor, T.D. Sands, Development of PZT and PZN-PT based unimorph actuators for micromechanical flapping mechanisms, in: Proceedings of the IEEE International Conference on Robotics and Automation, Seoul, Korea, May 2001.

[13] J.G. Smits, A. Ballato, Dynamic admittance of piezoelectric cantilever bimorphs, J. Microelect. Mech. Syst. 3 (3) (1994) 105–112.

[14] J.G. Smits, W.S. Choi, The constituent equations of piezoelectric heterogeneous bimorphs, IEEE Trans. Ultrasonics Ferroelect. Freq. Contr. 38 (3) (1991) 256–270.

[15] E.B. Tadfor, G. Kósa, Electromechanical coupling correction for piezoelectric layered beams, J. Microelect. Mech. Syst. 12 (6) (2003).

[16] Q.M. Wang, L.E. Cross, Constitutive equations of symmetrical triple layer piezoelectric benders, IEEE Trans. Ultrasonics Ferroelect. Freq. Contr. 46 (6) (1999) 1343–1351.

[17] Q.M. Wang, X.H. Du, B. Xu, L.E. Cross, Electromechanical coupling and output efficiency of piezoelectric bending actuators, IEEE Trans. Ultrasonics Ferroelect. Freq. Contr. 46 (3) (1999) 638–646.

[18] M.S. Weinberg, Working equations for piezoelectric actuators and sensors, J. Microelect. Mech. Syst. 8 (4) (1999) 529–533.

[19] R.J. Wood, R.S. Fearing, Flight force measurements for a micromechanical flying insect, in: Proceedings of the IEEE/RSJ International Conference on Intelligent Robots and Systems, Maui, HI, October 2001.

[20] R.J. Wood, S. Avadhanula, M. Menon, R.S. Fearing, Microrobotics using composite materials: the micromechanical flying insect thorax, in: Proceedings of the IEEE International Conference on Robotics and Automation, Taipei, Taiwan, September 2003.

[21] J. Yan, R.J. Wood, S. Avadhanula, M. Sitti, R.S. Fearing, Towards flapping wing control for a micromechanical flying insect, in: Proceedings of the IEEE International Conference on Robotics and Automation, Seoul, Korea, May 2001.

[22] G. Yang, S.-F. Liu, W. Ren, B.K. Mukherjee, Uniaxial stress dependence of the piezoelectric properties of lead zirconate titanate

ceramics, in: Proceedings of the 12th IEEE International Symposium 2000 on Applications of Ferroelectrics, 2001, pp. 431–434.
[23] J. Yin, B. Jiang, W. Cao, Elastic, piezoelectric, and dielectric properties of $0.995Pb(Zn_{1/3}Nb_{2/3})O_3$–$0.45PbTiO_3$ single crystal with designed multidomains, IEEE Trans. Ultrasonics Ferroelect. Freq. Contr. 47 (1) (2000) 285–291.
[24] K.J. Yoon, S. Shin, H.C. Park, N.S. Goo, Design and manufacture of a lightweight piezo-composite actuator, J. Smart Mater. Struct. 11 (2002) 163–168.

Biographies

Robert Wood is a PhD candidate in the Department of Electrical Engineering and Computer Sciences at the University of California, Berkeley. His research interests include biomimetic systems, microrobotics, micro air vehicles, and composite materials for microrobotic applications. He received his MS in EE from U.C. Berkeley (2001) and BS in EE from Syracuse University (1988).

Erik Steltz is a third year graduate student studying towards his PhD in the Department of Electrical Engineering and Computer Sciences at the University of California, Berkeley. He received a BS in Engineering Science from the Pennsylvania State University (2002). He has published in the area of electromagnetic behavior of thin films, but his current research focuses on biologically inspired robotics and millirobotics.

Ronald Fearing is a professor and vice chair for undergraduate matters in the Department of Electrical Engineering and Computer Sciences at University of California, Berkeley, which he joined in January 1988. His principal research interests are in micro robotics, including mobile micro-robots, dextrous micromanipulation and teletaction. He has a PhD from Stanford in EE (1988) and SB and SM in EECS from MIT (1983). He received the Presidential Young Investigator Award in 1991, and is the co-inventor on 2 US patents.